Escherichia coli 70 S ribosome at 15 Å resolution by cryo-electron microscopy: localization of fmet-tRNAfMet and fitting of L1 protein

ARTICLE · JANUARY 1998

CITATIONS
78

READS
22

9 AUTHORS, INCLUDING:

Arun Malhotra
University of Miami
54 PUBLICATIONS **1,937** CITATIONS
SEE PROFILE

Rajendra K Agrawal
Wadsworth Center, NYS Department of Hea…
74 PUBLICATIONS **3,046** CITATIONS
SEE PROFILE

Irene Gabashvili
28 PUBLICATIONS **1,442** CITATIONS
SEE PROFILE

Knud H Nierhaus
Charité Universitätsmedizin Berlin
348 PUBLICATIONS **11,205** CITATIONS
SEE PROFILE

Article No. mb981859 *J. Mol. Biol.* (1998) **280**, 103–116

JMB

Escherichia coli 70 S Ribosome at 15 Å Resolution by Cryo-electron Microscopy: Localization of fMet-tRNA$_f^{Met}$ and Fitting of L1 Protein

Arun Malhotra[1], Pawel Penczek[1,3], Rajendra K. Agrawal[1] Irene S. Gabashvili[1], Robert A. Grassucci[1], Ralf Jünemann[2] Nils Burkhardt[2], Knud H. Nierhaus[2] and Joachim Frank[1,3]*

[1]*Wadsworth Center, New York State Department of Health Empire State Plaza, PO Box 509, Albany, NY 12201-0509, USA*

[2]*Max-Planck-Institut für Molekulare Genetic AG Ribosomen, Ihnestr. 73 D-14195, Berlin, Germany*

[3]*Department of Biomedical Sciences, State University of New York at Albany, Empire State Plaza, PO Box 509 Albany, NY 12201-0509, USA*

**Corresponding author*

Cryo-electron microscopy of the ribosome in different binding states with mRNA and tRNA helps unravel the different steps of protein synthesis. Using over 29,000 projections of a ribosome complex in single-particle form, a three-dimensional map of the *Escherichia coli* 70 S ribosome was obtained in which a single site, the P site, is occupied by fMet-tRNA$_f^{Met}$ as directed by an AUG codon containing mRNA. The superior resolution of this three-dimensional map, 14.9 Å, has made it possible to fit the tRNA X-ray crystal structure directly and unambiguously into the electron density, thus determining the locations of anticodon-codon interaction and peptidyltransferase center of the ribosome. Furthermore, at this resolution, one of the distinctly visible domains corresponding to a ribosomal protein, L1, closely matches with its X-ray structure.

Keywords: ribosome structure; cryo-electron microscopy; tRNA P-site; polypeptide exit tunnel; L1 protein

Introduction

The ribosome is a large supramolecular complex that synthesizes protein according to genetic instructions provided by messenger RNA (mRNA). In this multi-step process, amino acid residues carried by transfer RNA (tRNA) are linked sequentially to form a polypeptide which subsequently exits the ribosome and folds into biologically active protein. Ribosome structure has been probed by a variety of methods over the past decades (reviewed by Green & Noller, 1997). Electron microscopy and immuno-electron microscopy (Oakes *et al.*, 1990; Stöffler-Meilicke & Stöffler, 1990; Frank *et al.*, 1990) have played an important role in these studies. Three-dimensional cryo-electron microscopy of single particles (Frank *et al.*, 1991; Frank, 1996) proved to be particularly powerful, showing the two subunits as distinct entities joined by several bridges, and enclosing a space (the intersubunit space) whose triangular shape suggested a unique placement of tRNA. As the technique was further developed, 20 to 25 Å density maps were obtained by two groups (Penczek *et al.*, 1994; Frank *et al.*, 1995a,b; Stark *et al.*, 1995) that provided a breakthrough in structural definition of the main features. Among the features relevant for the understanding of ribosomal function were a channel through the neck region of the 30 S subunit, postulated as the conduit for incoming mRNA (Frank *et al.*, 1995a,b), and a tunnel through the 50 S subunit that was thought to present the pathway for the outgoing newly synthesized polypeptide chain (reviewed by Eisenstein *et al.*, 1994). Subsequent work based on the availability of these maps has focused on the visualization of functional ligands *in situ* (tRNAs: Agrawal *et al.*, 1996; Stark *et al.*, 1997a; Agrawal *et al.*, unpublished results;

Present address: A. Malhotra, Department of Biochemistry & Molecular Biology, University of Miami School of Medicine, PO Box 016129, Miami, FL 33101-6129, USA.

Abbreviations used: 3D, three-dimensional; EM, electron microscopy; CTF, contrast transfer function; FSC, Fourier shell cross-correlation.

0022–2836/98/260103–14 $30.00/0

EF-Tu ternary complex: Stark *et al.*, 1997b; EF-G: Agrawal *et al.*, 1998) but with a resolution essentially limited to the 20 to 25 Å range.

In three-dimensional cryo-electron microscopy of single macromolecules (see Frank, 1996), the molecules are embedded in vitreous ice in random orientations, and imaged under low dose conditions in the electron microscope. A battery of mathematical techniques is used to determine the orientations of particles projections visible in the image, and to combine these projections in a three-dimensional density map.

Here we report a reconstruction based on a much larger data set of 29,324 projections covering a defocus range from 0.61 to 2.14 μm, of an initiation-like ribosome complex having mRNA with a unique AUG codon and fMet-tRNA$_f^{Met}$ in the P site. The resolution obtained, 14.9 Å, is the highest resolution achieved to date for an asymmetric structure by cryo-electron microscopy of single-particle specimens. The large number of particles is required because the structure contains no symmetry that could be used to increase the signal-to-noise ratio of high-resolution structural components by further averaging, as has been done for spherical viruses (Böttcher *et al.*, 1997; Conway *et al.*, 1997). Although the large size of the data set and the use of a defocus series is instrumental in realizing the 14.9 Å resolution, we have indications that this improvement is in large part due to the high occupancy of tRNA in the ribosome (>80%) which confers conformational stability to the specimen. Previous studies of naked ribosomes and low-occupancy ligand-ribosome complexes failed to give improvements that could be realized by increasing the particle number beyond the 5000 mark (Agrawal *et al.*, unpublished results).

New structural features are seen to emerge, and a much clearer delineation of a high-density ''backbone'' structure related to ribosomal RNA is observed when compared to earlier reconstructions by Frank *et al.* (1995a,b). The tRNA is directly visible in the three-dimensional reconstruction of the ribosome. The X-ray structure of the initiator tRNA (Basavappa & Sigler, 1991) was fitted into the 3D cryo-EM map, guided by molecular features such as helical grooves of the tRNA arms which are, for the first time, directly visible. Thus, the positions of the anticodon loop and the CCA acceptor end of the fMet-tRNA$_f^{Met}$ at the P-site tRNA could be determined with high accuracy.

The 50 S subunit tunnel previously seen (Frank *et al.*, 1995a,b) is well defined, and the close vicinity and orientation of the CCA end of the tRNA with respect to its mouth provide further support of the view (Frank *et al.*, 1995a,b) that this tunnel is the conduit for the nascent polypeptide chain. The much improved resolution of the three-dimensional map has also made it possible to obtain an interpretation of another portion of the ribosome on the atomic scale: the X-ray structure of the L1 protein from *Thermus thermophilus* (Nikonov *et al.*, 1996) closely matches and fits into the L1 region of the cryo-map.

Results and Discussion

Electron microscopy of fMet-tRNA$_f^{Met}$·ribosome complex

For the preparation of the fMet-tRNA$_f^{Met}$·ribosome complex, ribosomes programmed with a 46 nucleotide mRNA having a unique AUG start codon in the center were used. Aminoacylated and formylated tRNA (fMet-tRNA$_f^{Met}$) was added to form an initiation-like tRNA-ribosome complex (see Materials and Methods). Under the given conditions, the initiator tRNA binds at the P-site, a position where the first tRNA binds to initiate polypeptide synthesis on the prokaryotic ribosome. The use of a polyamine buffer system, along with an mRNA with a defined start codon allowed us to achieve a very high level of fMet-tRNA$_f^{Met}$ binding; 81% of the ribosomes had fMet-tRNA$_f^{Met}$ at the P-site (see Materials and Methods). This complex is referred to as ''high occupancy'' in this paper. To localize the tRNA binding site using difference maps, two additional complexes were also examined, naked 70 S ribosomes (control) and initiation-like tRNA-ribosome complex with a lower (42%) occupancy of fMet-tRNA$_f^{Met}$ (low-occupancy).

Image processing with CTF correction

The fMet-tRNA$_f^{Met}$·ribosome complexes were applied onto grids and flash frozen for cryo-electron microscopy. Micrographs with single particles of ribosomal complexes were used to construct a three-dimensional electron density map, using methods of 3D projection alignment, 3D reconstruction, and CTF correction, as described in Materials and Methods.

The Fourier transform of the intensity observed in a micrograph is modulated by the contrast transfer function (CTF) of the electron microscope (Zhu *et al.*, 1997), which is a periodic function of the resolution or frequency in Fourier space and is determined by the defocus setting used for collecting the images. These is rapid decay of the Fourier transform at spatial frequencies beyond the first zero of the CTF curve. A substantial increase in resolution can be obtained by combining data from different micrographs taken at different defocus settings which are chosen so that the zeros of the corresponding CTFs do not coincide. We used five defocus groups for the high-occupancy reconstruction, to achieve a resolution of 14.9 Å (using the Fourier shell correlation criterion with a 0.5 cutoff; see Appendix and the legend to Figure 1). For the low-occupancy reconstruction, two defocus groups were used to obtain a resolution of 19.5 Å, while a resolution of 25.4 Å was achieved for the control volume using a single defocus group. The recon-

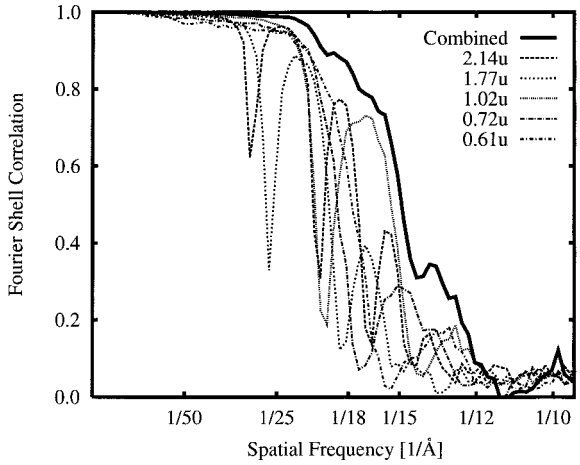

Figure 1. Assessment of the effective resolution of the high-occupancy 70 S·fMet-tRNA$_f^{Met}$ ribosome reconstruction. Fourier shell correlation curves for the five defocus series used in the cryo-map are shown as dotted lines. The curve obtained for the reconstruction from the merged data set is shown in bold. The presence of a sizeable lobe of information beyond 1/15 Å^{-1} indicates the potential of achieving a resolution of 12 Å.

structions agree in all major structural features when limited to a common resolution of 25.4 Å.

The resolution of these reconstructions was evaluated by randomly dividing the whole set of particles for each complex into halves. A 3D reconstruction was computed from each of these subsets, and the Fourier shell cross-correlation (FSC) between the two volumes was used as an indication of effective resolution (Figure 1). The FSC curve can be interpreted in different ways (see Appendix). A conservative approach (Böttcher *et al.*, 1997; Conway *et al.*, 1997) uses an FSC of 0.5 as the effective resolution of the reconstruction, while the three-sigma FSC criterion (Harauz & van Heel, 1986) uses a cutoff value that is close to zero in the interesting resolution range. Using an FSC criterion with a 0.5 cutoff, we estimate a resolution of 14.9 Å for the high-occupancy reconstruction. The use of the three-sigma criterion results in an estimate of 11.75 Å, close to the Nyquist frequency limit of 9.56 Å (for a sampling distance of 4.78 Å), which is rarely attained.

While the choice of the FSC cutoff criteria is somewhat arbitrary, an independent measure of the effective resolution should be provided by the cryo-EM map itself: the effective resolution of a reconstruction should be reflected in the structural details that can be visualized. In the high-occupancy reconstruction, we see details that are expected of a 15 Å map in two regions that were fitted with atomic models: the L1 protein and the P-site tRNA. For example, when simulated electron density for two large RNAs: initiator tRNA (Basavappa & Sigler, 1991; Figure 4(b), below) and the p4-p6 ribozyme RNA (Cate *et al.*, 1996; not shown) whose atomic structures are known, is limited to 15 Å in resolution, the RNA helices appear as long cylinders with major groove indentations visible at high thresholds. When properly filtered and thresholded, such features can be seen in the high-occupancy cryo-EM reconstruction as discussed below (Figures 4 and 5, below). At the same time, we do not see molecular details expected of an electron density map that extends to 12 Å, such as a clear distinction between L1 protein structural domains, indicating that the conservative resolution measure used here is appropriate. A similar correspondence between effective resolution based on an FSC cutoff of 0.5 and structural detail was seen in two other recent cryo-EM structures of symmetric virus assemblies which have been solved to a resolution of better than 10 Å (Böttcher *et al.*, 1997; Conway *et al.*, 1997).

While the correspondence between the FSC resolution and the observed details is reassuring, this measure underestimates resolution somewhat because it compares volumes generated from only half the number of particles used for the full 3D reconstruction. It should also be noted that FSC is a global rather than a local measure of resolution, and includes regions that are well resolved along with parts of the map that may be more poorly defined because of the conformational variability of local features.

Structure of the initiation-state 70 S ribosome

Figure 2(a), (c) and (d) shows three different views of the high-occupancy 70 S·fMet-tRNA$_f^{Met}$ complex reconstructed as a surface view. Viewed with the two subunits side-by-side, the tRNA mass can be clearly seen in the intersubunit space of the high-occupancy complex (Figure 2(a)) when compared with the low-occupancy reconstruction where the tRNA has a lower average density and is therefore invisible at the normal display threshold (Figure 2(b)). The increased resolution of the high-occupancy reconstruction allows new features to be discerned in both surface views (Figure 2), as well as in the interior of the ribosome (Figures 4 and 5, below). Among the new surface features brought out by the improved resolution that were not seen before are the two-domain structure of the 30 S subunit platform (pt1, pt2 in Figure 2(d)), the distinct triangular shape of the L1 protein (Figure 2(c) and (d), a sharp beak, a beaded thread-like structure on the back of the 30 S subunit (bt in Figure 2(a)), and a curved ''long bridge'' (1b) connecting the two subunits (Figure 2 (a) and (c)). The long bridge is an extension of a shorter protrusion seen in the earlier 25 Å cryo-EM map (Frank *et al.*, 1995a,b), which was termed ''A-side finger'' by Stark *et al.* (1997a) because of its close proximity to the A-site tRNA. The channel running through the neck of the 30 S subunit, previously interpreted as an mRNA pathway (Frank *et al.*, 1995a,b; Agrawal *et al.*, 1996; Lata *et al.*, 1996), opens up further (not shown) in the current recon-

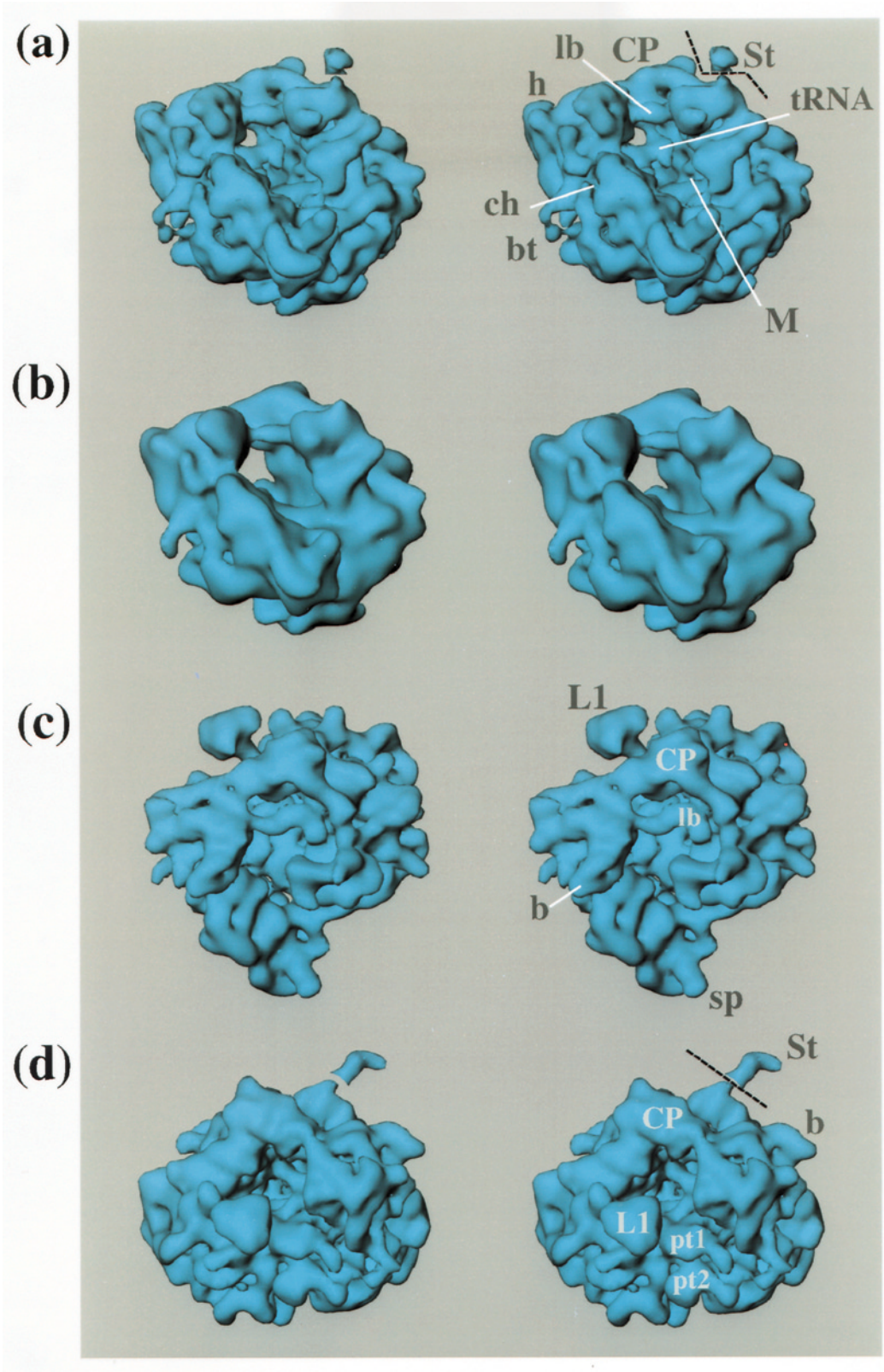

Figure 2. Shaded stereo surface representations of the 70 S·fMet-tRNA$_f^{Met}$ ribosome complex presented from different viewing directions. (a), (c), (d) The 14.9 Å high-occupancy reconstruction. (a) Frontal view showing tRNA as a partial occlusion of the intersubunit space; (b) low-occupancy map, presented at 19.5 Å resolution, showing the absence of tRNA in the intersubunit space; (c) top view showing the long bridge (lb), and the L1 protein region (L1); (d) view of the 14.9 Å map from the L1 and 30 S subunit platform side. Landmarks of the 30 S subunit: h, head; ch, channel entrance; b, beak; bt, beaded thread loop; sp, spur; pt1, pt2, two prominent domains of platform. Landmarks of the 50 S subunit: St, extended portion of stalk visible with reduced threshold, indicated by a broken line in (a) and (d); CP, central protuberance; L1, L1 protein; M, tunnel mouth. In all panels, except (d), the 30 S subunit is on the left side of the reconstruction.

struction. This channel leads into the intersubunit space close to the anticodon end of the P-site tRNA (see below).

The L7/L12 stalk is known to be a flexible, highly mobile component of the ribosome (e.g. see Traut *et al.*, 1995). In earlier cryo-EM reconstructions of the naked ribosome (Frank *et al.*, 1995a; Stark *et al.*, 1995), it was observed in a folded-up conformation. However, in our previous tRNA binding study, it showed up in an extended form (Agrawal *et al.*, 1996). In the current reconstruction, the extended form is again observed when the display threshold is lowered (Figure 2(a) and (d)). The reason why the stalk is not seen at normal threshold could be explained in the following way: if one assumes that tRNA binding has a stabilizing effect on the stalk position, then only 81% of the stalks would contribute to the map in a consistent way, but even small residual variations would tend to further reduce and blur the density at this location.

At higher threshold, the interior of the ribosome resolves into strands that are continuous in most parts. Although it is still not possible, at the current resolution, to distinguish RNA from protein unambiguously on the basis of density, the diameter of these strands, in the range of 20 Å, suggests that they present double-stranded rRNA regions. Previous modeling efforts based on cross-linking, chemical protection, and immuno-EM studies that used data from maps derived from EM (Malhotra & Harvey, 1994; Mueller & Brimacombe, 1997) have been hampered by the inability to directly visualize RNA regions; the current 14.9 Å cryo-EM map for the first time provides a basis for building ribosome models that follows RNA strands directly.

Location of tRNA in the P-site

To carefully localize the P-site tRNA, difference maps between the different reconstructions were computed. The difference map obtained by subtraction of the naked control from the high-occupancy complex (Figure 3(a), red) is expected to show both mRNA and tRNA, while a difference map between the high and low-occupancy reconstructions (Figure 3(b), green) should reveal the tRNA position, since these two complexes differ in the weight of the tRNA mass, but have the same mRNA occupancy. The mass attributable to tRNA (Figure 3(b), green) is clearly L-shaped, pointing with the short CCA-bearing arm toward the mouth of the 50 S subunit tunnel (marked as M in Figure 2(a), see below) and with the long (anticodon) arm towards the small subunit cleft. How-

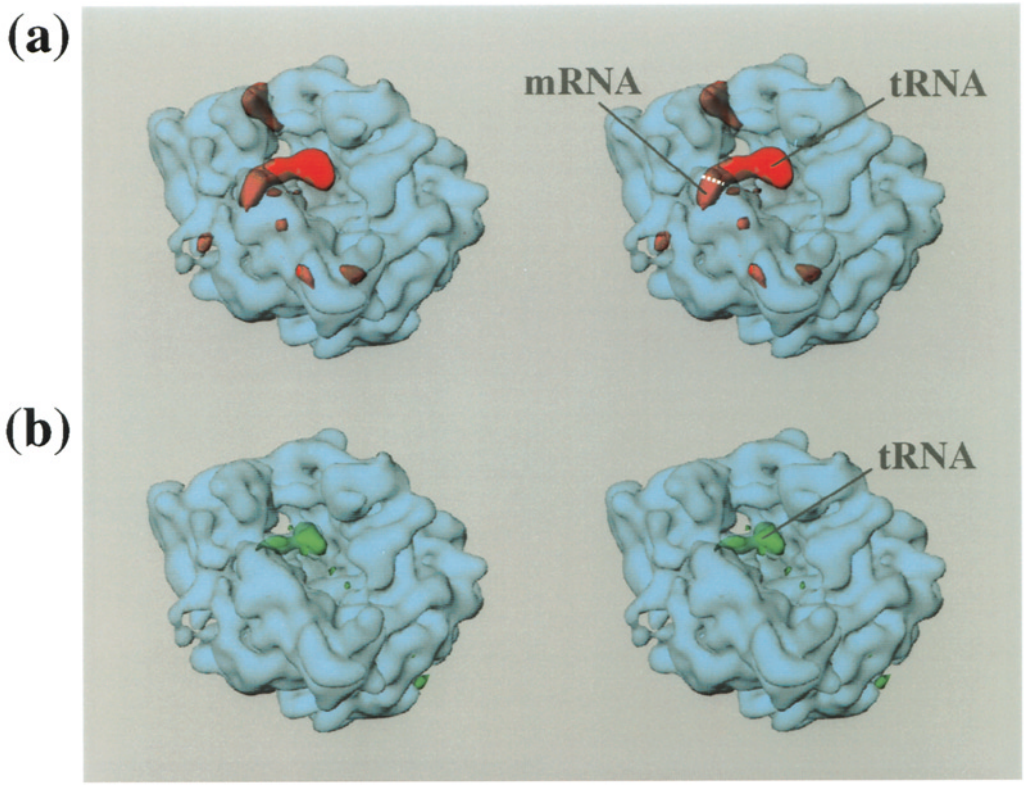

Figure 3. Identification of the 70 S ribosome P-site using difference maps displayed on a semi-transparent version of the 14.9 Å reconstruction (Figure 2(a)), shown in stereo surface representations. (a) Difference map obtained by subtraction of the control from the high-occupancy reconstruction, limited to 25.4 Å resolution, showing a difference peak attributed to tRNA and mRNA, as well as other peaks related to conformational changes; (b) difference map obtained by subtraction of low from high-occupancy reconstructions, presented at 19.5 Å resolution.

ever, this mass is smaller than expected for complete visualization of tRNA, presumably because some parts of the structure are not stabilized by rRNA interactions. The mass identified in Figure 3(a) as tRNA is extended at the anticodon end, in the region where mRNA-tRNA interaction takes place. This indicates that the extra mass of density at the anticodon end is due to the mRNA. Density corresponding to the rest of the 46 nucleotide mRNA is not seen, presumably because of positional flexibility of the flanking upstream and downstream regions. Other difference peaks outside the intersubunit space (Figure 3(a)) in the high-occupancy minus naked control difference map are also seen in the low-occupancy minus control map (not shown). These highly reproducible difference peaks are due to conformational differences between the tRNA-ribosome complex and the naked ribosome (Agrawal *et al.*, unpublished results).

Since the low-occupancy reconstruction has an estimated resolution of 19.5 Å, the difference map shown in Figure 3(b) is limited in effective resolution to less than 19.5 Å, and does not fully exploit the resolution of the high-occupancy cryo-EM map. We thus used the difference map to guide us into the region of the high-occupancy reconstruction corresponding to the P-site tRNA; this region of the cryo-EM map was then used directly to fit the initiator $tRNA_i^{Met}$ X-ray structure (Basavappa & Sigler, 1991). For the fitting, the cryo-EM map was filtered to enhance high resolution features in the 20 to 15 Å range and was displayed at a high threshold. Under these conditions only the regions of high electron density, corresponding to the center of RNA helices or compact protein cores, can be seen (Figures 4 and 5). The proper fit of the $tRNA_i^{Met}$ X-ray structure was facilitated by the helical groove features that can be seen in the cryo-EM map (Figure 4(a)). These helical grooves restrict the range of possible tRNA positions to only about 1 to 2 Å, allowing a very precise localization of the P-site tRNA. The visualization of such features is expected at a resolution of 15 Å, as can be seen in Figure 4(b), which shows the density expected for $tRNA_i^{Met}$ if X-ray diffraction data were available only to 15 Å. No density was seen for the CCA end of the tRNA, and only weak density was seen for part of the tRNA D-loop and the anticodon loop. This may indicate some flexibility or conformational heterogeneity in these regions of the tRNA in the P site. The $tRNA_i^{Met}$ X-ray structure also showed disorder at the end of the anticodon stem-loop (Basavappa & Sigler, 1991). While some additional density is seen near the anticodon stem (Figure 3(a) and 4(a)), the anticodon-mRNA interaction cannot be precisely localized in the cryo-EM map.

The P-site tRNA density in the high-occupancy map is connected with density for the 70 S ribosome at four locations, as shown in Figure 4(a)), indicating that these regions are involved in intimate contacts with ribosomal RNA/protein components. These regions are centered on the backbone of G57 on the tip of the tRNA elbow, G12·C23 base-pair on the D stem below the inner bend, and U33 and A37 in the anticodon loop. The density from the anticodon loop extends into the 30 S body near the platform at the lower end (arrow marked in Figure 4(a), and the 30 S head (arrow marked in Figure 4(a)), while the contact from the tRNA elbow extends to the 50 S central protuberance. The contact at the G12·C23 base-pair extends and splits into strands which connect with both the 50 S body at the interface canyon and the 30 S platform. The density from the G12·C23 base-pair extends from the minor groove in this region, and may include ribosomal RNA interactions with the tRNA bases. The regions near the elbow and anticodon can accommodate both backbone and base interactions. These connections between the P-site tRNA and ribosome density include (or are sufficiently close to) most of the nucleotides in tRNA that have been cross-linked to ribosomal components (Döring *et al.*, 1994; Rosen & Zimmermann, 1997; and others reviewed by Wower *et al.*, 1993). Osswald *et al.* (1995) show cross-links from nucleotide 47 on tRNA in the P-site to several ribosomal components. While no direct density to the ribosomal subunits is seen at this site, several regions of both 50 S and 30 S subunits are close enough for the ~15 Å span of the diazirine cross-linker used in their study. The tRNA-ribosome contact points, and areas of close proximity, agree with data from experiments probing P-site tRNA chemical accessibility (Dabrowski *et al.*, 1995). These experiments also find the region around nucleotide 47 of P-site tRNA to be unprotected, consistent with our results.

The tRNA partially overlaps with the previously inferred position of the deacylated $tRNA^{Phe}$ in the P-site position (Agrawal *et al.*, 1996); however, the anticodon is shifted toward the L1 protein and lies in the cleft of the 30 S subunit, and the elbow is shifted towards the interface canyon and the L7/L12 stalk of the 50 S subunit. Although the earlier observation (Agrawal *et al.*,1996) was made at lower resolution (25 Å), these results clearly show that the deacylated and aminoacylated tRNAs acquire different positions in the P-site (Agrawal *et al.*, unpublished results). The P-site position inferred by others (Stark *et al.*, 1997a) from tRNA-ribosome complexes in pre and post-translocation configuration appears to be close to that obtained here. However, unlike previous studies (Agrawal *et al.*, 1996; Stark *et al.*, 1997a), the present results allows the P-site tRNA to be positively and unambiguously identified, providing a landmark for rRNA modeling and ribosomal protein positioning based on available chemical protection, cross-linking (reviewed by Brimacombe, 1995; Green & Noller, 1997), and immuno-electron microscopy data (reviewed by Stöffler-Meilicke & Stöffler, 1990).

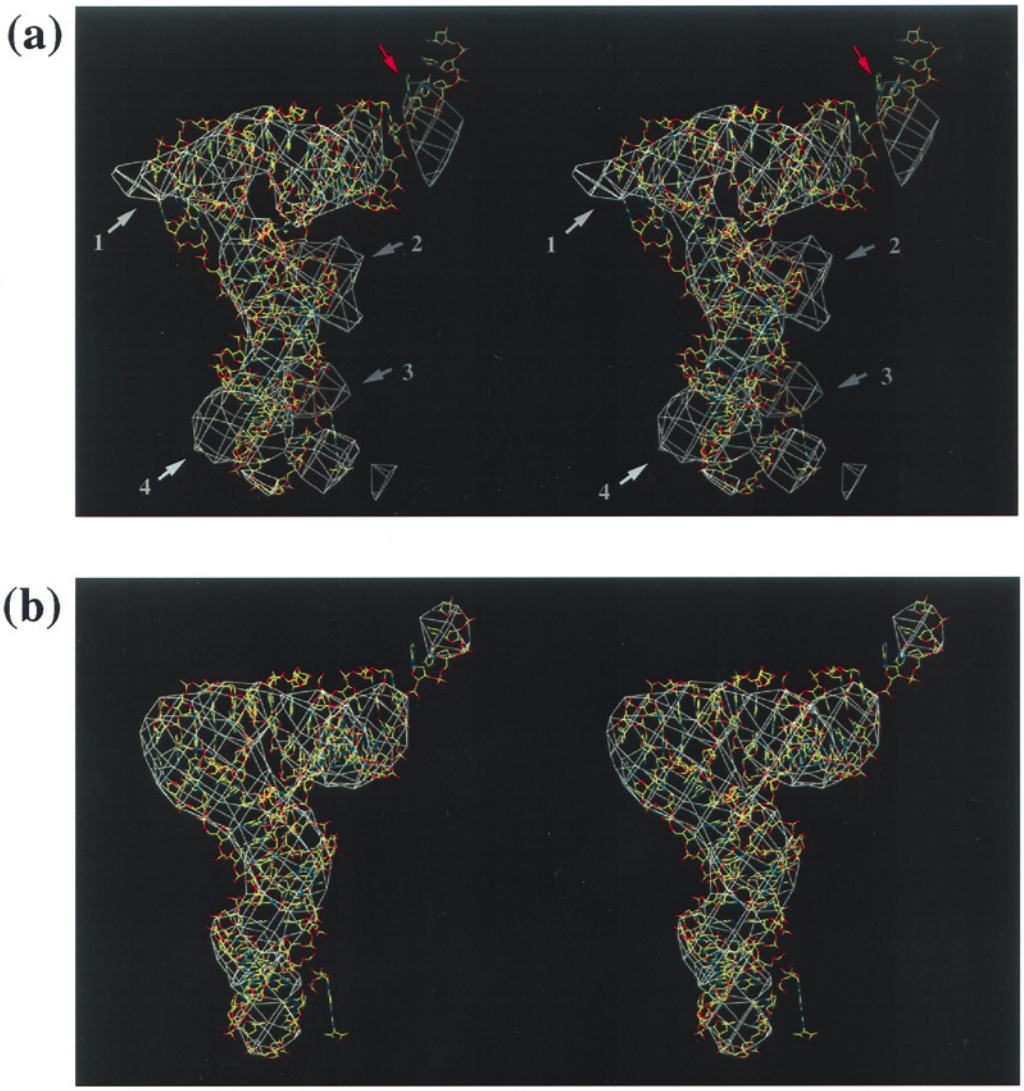

Figure 4. Positioning of the initiator tRNA into the 70 S·fMet-tRNA$_f^{Met}$ complex cryo-EM map. (a) Stereo view of the P-site region of the high-occupancy cryo-EM map, fitted with the X-ray crystal structure of the initiator tRNA (Basavappa & Sigler, 1991). The cryo-EM map shown is filtered to enhance frequencies in the 20 to 15 Å resolution range and is displayed at a high threshold (white). Only ribosome regions within 10 Å of the initiator tRNA atomic structure are shown for clarity. The numbered arrows in grey point to strands of density that extend from the electron density corresponding to the P-site tRNA into the 30 S subunit (bottom) and the 50 S subunit (top and right): 1 centered on tRNA nucleotide 57; 2, centered on base-pair 12 to 23; 3, close to nucleotide 37; and 4, close to nucleotide 33. The red arrow points to density from the 50 S subunit close to, but not enclosing, the acceptor end of the tRNA. (b) Stereo view of the X-ray structure of the initiator tRNA (Basavappa & Sigler, 1991) shown with electron density (white) computed from the atomic coordinates, limited to a resolution of 15 Å, using the program X-PLOR (Brünger, 1992). The view shown is in the same orientation as in (a). Both panels show electron density using the program O (Jones *et al.*, 1991) contoured at 2.2σ using maps from (a), cryo-EM; and (b), X-ray crystal structure atomic coordinates, that have been normalized to an average density of zero, and a standard deviation of 1 (Kleywegt & Jones, 1996).

Fitting of L1 X-ray crystal structure

L1 is the second largest protein in the 50 S subunit, and has been localized by immuno-EM studies (reviewed by Stöffler-Meilicke & Stöffler, 1990) to the left edge of the 50 S subunit as viewed from the subunit interface. While L1 is dispensable for cell viability and protein synthesis, *Escherichia coli* mutants lacking L1 show a twofold reduction in the rate of protein synthesis (Subramanian & Dabbs, 1980). Other experiments have shown that L1 may be involved in interactions with tRNAs during proteins synthesis (Rosen *et al.*, 1993; Agrawal *et al.*, 1996, and unpublished results).

In the 70 S·fMet-tRNA$_f^{Met}$ complex cryo-map, the region corresponding to the 50 S subunit protein L1 (Figures 2(c), (d) and 5(a)) has the shape of a mushroom, and is triangular in outline when viewed from above (Figure 2(d)). It is connected to the body of the 50 S subunit by a cylindrical stem.

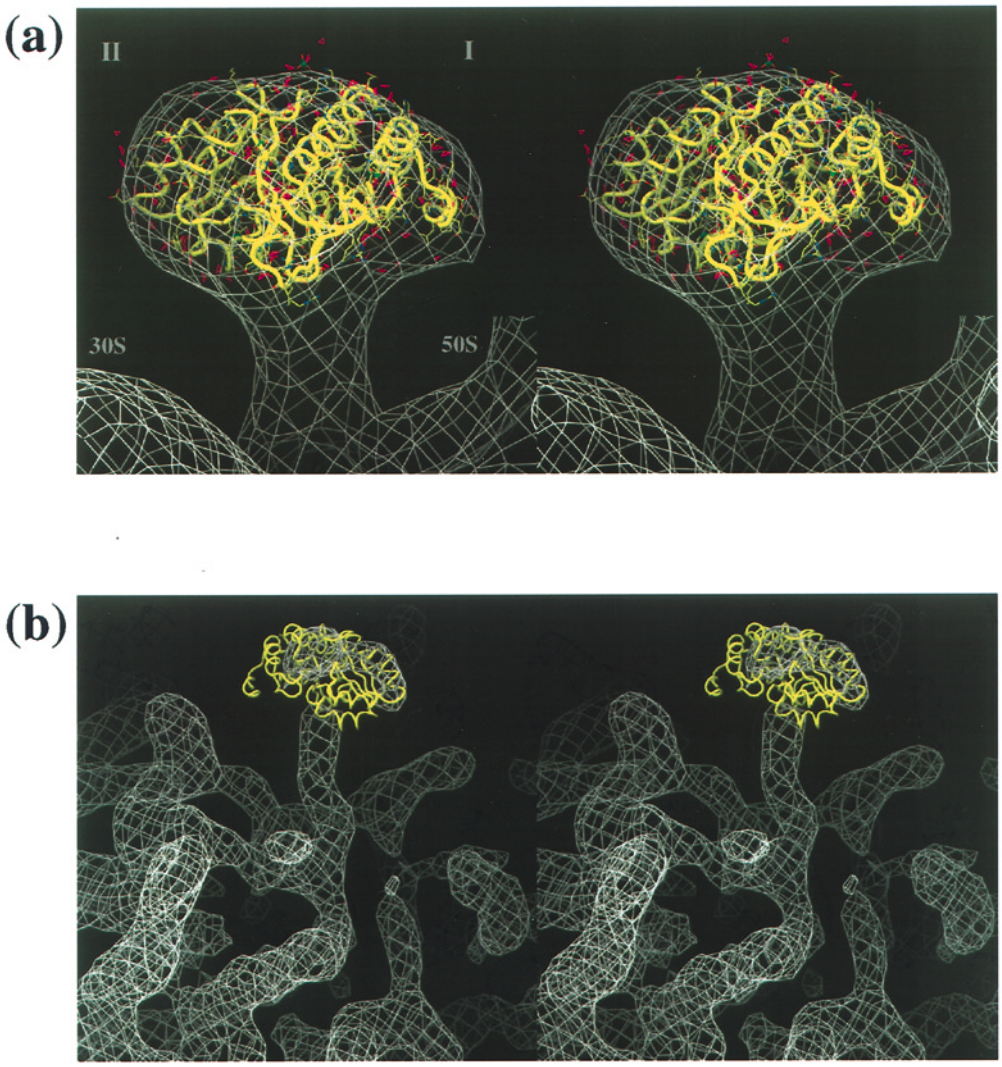

Figure 5. Fitting the L1 X-ray crystal structure into the 70 S·fMet-tRNA$_f^{Met}$ complex high-occupancy cryo-EM map. (a) Stereo view of the L1 region of the 50 S subunit of *E. coli* ribosome (white), fitted with the X-ray structure of L1 from *T. thermophilus* (Nikonov *et al.*, 1996) shown with a tube along the backbone, side-chains and solvent molecules. The domains I and II are marked (notation by Nikonov *et al.*, 1996). The view shown is from the interface canyon, with the 50 S subunit on the right. (b) Stereo view of the ribosome region in the vicinity of the L1 protein (shown as a tube in yellow). The cryo-map shown is filtered to enhance frequencies in the 20 to 15 Å resolution range and is displayed at a high threshold (white). The strand continuous with the stem of L1 is interpreted as primarily rRNA. The view shown is rotated by approximately 180° around the vertical axis from the view in (a).

The shape and dimensions of the globular mass supported by the stem closely agree with those of L1 from *Thermus thermophilus* as obtained by X-ray crystallography (Nikonov *et al.*, 1996). This structure includes the full length of L1, except for the first eight N-terminal residues. L1 proteins from *E. coli* and *T. thermophilus* are similar in size (233 *versus* 228 amino acids) and share 50% sequence identity (73% similarity), which indicates close similarity in their structures. The X-ray structure of *T. thermophilus* was docked manually, guided by cross-correlation between the cryo-EM map and the electron density of the protein's atomic structure. This docking is tightly restricted by the semi-concavity of the cryo-EM map (Figure 2(c)), which agrees with the semi-concave shape of the X-ray structure.

Electron density computed from the X-ray structure coordinates of L1 lacks molecular features such as helices and sheets when limited to 15 Å in resolution. However, at that resolution two unequal regions of higher density can be discerned corresponding to the cores of the two main domains of L1. The ribosome cryo-EM map, when viewed at higher thresholds, also shows two regions of higher density that have unequal size. The separation between these regions and their relative sizes are similar to these features in the 15 Å limited electron density from the X-ray structure.

Residues of L1 implicated in rRNA interactions lie in the highly conserved, positively charged inter-domain region of the proteins (Nikonov *et al.*, 1996), and in our fitting this region indeed comes to lie facing the cylindrical stalk that connects the L1 density to the body of the 50 S subunit. The consensus L1 binding site on 23 S rRNA corresponds to an internal loop near nucleotide 2160 bounded by two helical segments, but the precise arrangement of this region is not known (Nikonov *et al.*, 1996). However, the diameter of the L1-carrying stem (20 Å) matches quite closely with that of ideal A-form double-stranded RNA (Arnott *et al.*, 1976). This stem can be seen even at higher threshold, and extends as a continuous strand of density into the body of the 50 SD subunit (Figure 5(b)) for several hundred Å. This putative rRNA strand probably reflects the location of helices 75 to 78 in domain V of the 23 S RNA (notation by Leffers *et al.*, 1987) in the 50 S subunit.

The threshold, used in Figure 5(a), that yields an L1 envelope which matches closely with the L1 atomic structure corresponds to a ribosome volume of 2.8×10^6 Å^3. This volume is close to the volume 2.4×10^6 Å^3, expected based on the chemical molecular mass of the 70 S ribosome (Zhu *et al.*, 1997). Ribosomal volumes computed from cryo-EM are very sensitive to the threshold levels used to display the electron density, and various rationales have been used to choose appropriate threshold values in previous reconstructions (Zhu *et al.*, 1997; Stark *et al.*, 1995; see also the discussion by Frank & Agrawal, 1998). The fit of an atomic structure provides an independent guideline for the choice of threshold level, and it is encouraging that the threshold value that provides a good fit to the L1 atomic structure also correctly corresponds to the expected volume of the ribosome. Since the solvent content of L1 was not considered in the cryo-EM map fitting, a threshold value slightly lower than that used in Figure 5(a) will correspond to the fully hydrated ribosomal mass.

Polypeptide exit tunnel

A tunnel through the large subunit was observed in several earlier studies using 3D EM of ribosomes from prokaryotes (Yonath *et al.*, 1987) and eukaryotes (Milligan & Unwin, 1986), and was postulated to serve as conduit through which the nascent polypeptide exits the ribosome (see Eisenstein *et al.*, 1994). Such a tunnel, leading from the bottom of the interface canyon of the 50 S subunit to the site found by immuno-EM of the nascent chain (Bernabeu & Lake, 1982), has been identified in our earlier cryo-map of the *E. coli* ribosome (Frank *et al.*, 1995a) and, in identical positions, in subsequent cryo-maps of ribosomes from yeast (Beckmann *et al.*, 1997; Verschoor *et al.*, 1998) and *Haloarcula marismortui* (Frank *et al.*, unpublished results). The interpretation of this tunnel as the conduit for the nascent polypeptide has recently been bolstered by the observation that the Sec61 protein conducting channel complex aligns directly its exit site on the yeast ribosome (Beckmann *et al.*, 1997). The close spatial association of the tunnel mouth with the acceptor end of the P-site tRNA observed in the current reconstruction (Figure 6(a)) provides additional strong support for this hypothesis.

The 50 S subunit tunnel is now much better defined and can be seen as a continuous channel even at normal levels of threshold (Figure 6(b)). It starts with its mouth (M) in the interface canyon near the CCA end of the P-site tRNA and exits at the bottom of the subunit (EX1: Figure 6(b)). Its linear length is 71 Å, and its width is between 16 and 19 Å, providing ample space to accommodate the nascent polypeptide chain in an extended or α-helical configuration. The tunnel communicates with several blind cavities within the 50 S subunit. Its main connection is to a circular tube that exits at a distance of 53 Å from EX1, at the site (EX2) identified previously (Frank *et al.*, 1995a,b) as the second tunnel exit site. Thus, what previously appeared as a secondary tunnel running with a 90° angle to the primary tunnel, communicating with a side compartment, is now resolved into a more complex tubular system.

Conclusions

The 14.9 Å resolution three-dimensional reconstruction of the fMet-tRNA$_f^{Met}$·ribosome complex presented here is the highest resolution achieved to date for an asymmetric macromolecular complex by single-particle microscopy. At this resolution, we have been able to assign the P-site position of tRNA with high accuracy, and are just beginning to discern protein domains, active sites, and rRNA strands that comprise the ribosome. The close correspondence between structural details as seen at low resolution by single particle cryo-EM and at high resolution by X-ray crystallography, illustrated here gives support to the use of these techniques for deciphering the molecular details of the translational machinery. There are encouraging signs (see Figure 1) that even higher resolutions of 12 Å or better may be achieved with cryo-EM using more particles and an extended defocus range.

As evidenced here even at 15 Å resolution, enough detail can be seen to directly visualize RNA strands, though interpretation is complicated by the intimate mix of proteins and RNA that form the ribosome. In general, RNA helical segments can be visualized as separate entities at resolutions lower than necessary for assignment of protein structures which are composed of more disparate structural elements. The presence of deep major grooves in regular duplex RNA is another feature that can begin to be visualized at this resolution, providing a very precise marker for RNA placement. While previous efforts (Malhotra & Harvey, 1994; Mueller & Brimacombe, 1997; and others) have combined modeling and intuition with EM and biochemical data, the current 14.9 Å cryo-EM

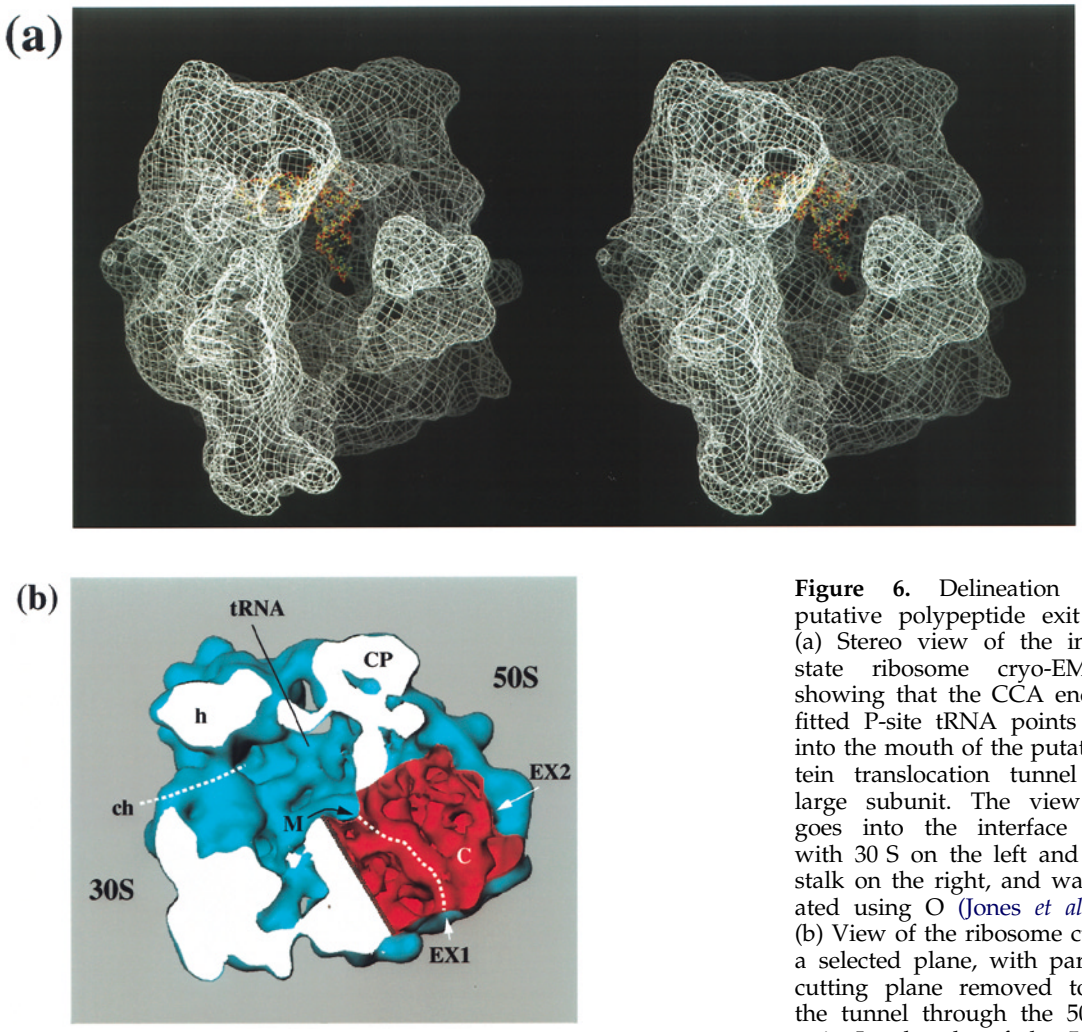

Figure 6. Delineation of the putative polypeptide exit tunnel. (a) Stereo view of the initiation-state ribosome cryo-EM map, showing that the CCA end of the fitted P-site tRNA points directly into the mouth of the putative protein translocation tunnel in the large subunit. The view shown goes into the interface canyon, with 30 S on the left and L7/L12 stalk on the right, and was generated using O (Jones *et al.*, 1991). (b) View of the ribosome cut along a selected plane, with part of the cutting plane removed to reveal the tunnel through the 50 S subunit. Landmarks of the 50 S subunit: M, tunnel mouth; EX1, primary exit site; EX2, secondary site (this nomenclature was chosen to avoid confusion with the tRNA exit site (E site). Thus, E1 and E2 of Frank *et al.*, (1995a,b) are now termed EX1 and EX2, respectively); C, circular side tunnel; CP, central protuberance. Landmarks of the 30 S subunit: h, head; ch, channel.

map, with future improvements, provides the first electron density into which ribosomal RNA can be directly assigned, a task made easier by the well established rRNA secondary structure and the wealth of low-resolution biochemical data on rRNA-rRNA and rRNA-proteins interactions (Brimacombe, 1995).

Materials and Methods

Preparation of fMet-tRNA^{Met}·ribosome complexes

Initiation-like ribosomal complexes were prepared by binding an fMet-tRNA$_f^{Met}$ to the P-site of ribosomes programmed with a 46 nucleotide mRNA fragment (MF-mRNA) that carries a unique AUG codon in its middle. Tightly coupled 70 S ribosomes were prepared according to Bommer *et al.* (1997). The MF-mRNA was prepared by *in vitro* T7 run-off transcription (Wadzack *et al.*, 1997). tRNA$_f^{Met}$ (Subriden, Rolling Bay) was aminoacylated, formylated and purified following the protocol of Jünemann *et al.* (1996) except that tRNA was protonated and ^{35}S-labelled methionine was used. The resulting f-[^{35}S]Met-tRNA$_f^{Met}$ displayed a purity of 1650 pmol/A_{260} unit. f-[^{35}S]Met-tRNA$_f^{Met}$ binding to MF-mRNA programmed ribosomes was performed in binding buffer conditions (20 mM Hepes/KOH, 6 mM $Mg(CH_3COO)_2$, 150 mM NH_4Cl, 4 mM β-mercaptoethanol, 0.05 spermine, 2 mM spermidine (Bommer *et al.*, 1997) with either 0.75 (low occupancy) or threefold (high occupancy) molar excess of ribosomes. The non-bound tRNA was quantitatively removed from the ribosomal complexes by gel filtration over Sephacryl-S300 cDNA spun column (Pharmacia, Sweden) equilibrated with binding buffer (one minute at 4°C, 1500 rpm, HB4 rotor). The binding level in the final complexes was 42% and 81%, respectively; P-site location of the f-[^{35}S]Met-tRNA$_f^{Met}$ was 100% in both cases as determined by the puromycin reaction (Bommer *et al.*, 1997). Both complexes yielded an homogeneous 70 S peak in the analytical sucrose density gradient.

Electron microscopy

Grids were prepared for cryo-microscopy according to standardized methods (Wagenknecht *et al.*, 1988;

Dubochet *et al.*, 1988). Micrographs were recorded using low-dose protocols on a Philips EM420 electron microscope at a magnification of 52,200 × (±2%) as checked by a tobacco mosaic virus standard.

Image processing

Micrographs were checked for drift, astigmatism, and presence of Thon rings by optical diffraction. Scanning was done with a step size of 25 μm corresponding to 4.78 Å on the object scale, on a Perkin Elmer PSD 1010A microdensitometer. A total of 62 micrographs were used, grouped into five defocus settings: 0.61, 0.72, 1.02, 1.77, and 2.14 μm. Ribosomes were selected by an automated selection procedure that differed from the one previously described (Lata *et al.*, 1995) in that the particle candidates were directly compared with the reference set of 87 quasi-evenly spaced projections (Penczek *et al.*, 1994) of an existing best-resolution reconstruction (S. Srivastava, R. K. Agrawal, P.P., R.G. & J.F., unpublished results). For each defocus group, particles were rejected based on the value of the cross-correlation coefficient. Thus, of the 47,265 particles initially picked, a total of 29,324 were identified by orientation and selected for further processing. For each defocus group, one step of the 3D projection alignment procedure (Penczek *et al.*, 1994) was applied and a merged, CTF-corrected reconstruction was computed as described (Zhu *et al.*, 1997). Starting each time with the CTF-modified reconstruction of the previous step, this refinement was repeated three times using a 2.0° angular step, and then twice using a 1.5° step for increased accuracy. In each step, the refined 3D structure was calculated using 90% of the best matching particles (based on the value of the cross-correlation coefficient). Control and low-occupancy reconstructions were computed similarly from 4518 particles (13 micrographs at 1.8 μm defocus) and 9429 particles (24 micrographs at 1.0 and 1.8 μm defocus), respectively. In contrast to the high-occupancy reconstruction, inclusion of additional data failed to improve the resolution in the reconstructions from these data sets.

To test whether the choice of the initial reference volume biases our refinement procedure, two 3D reconstructions were performed. The first used for defocus groups, yielding a 3D reconstruction with a resolution of 15.3 Å. This was drastically low-pass Fourier filtered to eliminate features with resolution higher than 48 Å and used as a bias-free reference for the full reconstruction with five defocus groups. The final resolution, estimated using the FSC with a cutoff value of 0.5 (Böttcher *et al.*, 1997) was 14.9 Å (see Figure 1). Excellent agreement extending beyond 14.5 Å (as measured by FSC) was seen between the reconstructions from four defocus groups and five defocus groups, indicating that there was no discernible influence of the initial reference volume on our refinement procedure.

Acknowledgments

We thank Seth Darst, the Rockefeller University, for making an SGI Origin 2000 available for some of the computation, and Doryen Bubeck and Amy Heagle for assistance with image processing and illustrations. We are grateful to Paul Masters for valuable suggestions. We also thank Anders Liljas, University of Lund, for providing the coordinates of L1. This work was supported by grants from the National Institutes of Health (R01-GM29169) and the National Science foundation (BIR9219043). A.M. and P.P. contributed equally to this work.

References

Agrawal, R. K., Penczek, P., Grassucci, R. A., Li, Y., Leith, A., Nierhaus, K. H. & Frank, J. (1996). Direct visualization of A-, P-, and E-site transfer RNAs in the *Escherichia coli* ribosome. *Science,* **271**, 1000–1002.

Agrawal, R. K., Penczek, P., Grassucci, R. A. & Frank, J. (1998). Visualization of elongation factor G on the *Escherichia coli* 70 S ribosome: the mechanism of translocation. *Proc. Natl Acad. Sci. USA,* **95**, 6134–6138.

Arnott, S., Campbell, Smith P. J. & Chandrasekaran, R. (1976). Atomic coordinates and molecular conformations for DNA-DNA, RNA-RNA, and DNA-DNA helices. In *Handbook of Biochemistry and Molecular Biology* (Fasman, G. D., ed.), pp. 411–422, CRC Press, Cleveland, OH.

Basavappa, R. & Sigler, P. B. (1991). The 3 Å crystal structure of yeast initiator tRNA: functional implications in initiator/elongator discrimination. *EMBO J.* **10**, 3105–3111.

Beckmann, R., Bubeck, D., Grassucci, R., Penczek, P., Verschoor, A., Blobel, G. & Frank, J. (1997). Three-dimensional reconstruction of the ribosome-Sec61 complex revealing alignment of conduits for nascent polypeptide chain. *Science,* **278**, 2123–2126.

Bernabeu, C. & Lake, J. A. (1982). Nascent polypeptide chains emerge from the exit domain of the large ribosomal subunit: immune mapping of the nascent chain. *Proc. Natl Acad. Sci. USA,* **79**, 3111–3115.

Bommer, U., Burkhardt, N., Jünemann, R., Spahn, C. M. T., Triana-Alonso, F. J. & Nierhaus, K. H. (1997). Ribosomes and polysomes. In *Subcellular Fractionation: A Practical Approach* (Graham, J. & Rickwood, D., eds), pp. 271–301, IRL Press, Washington, DC.

Böttcher, B., Wynne, S. A. & Crowther, R. A. (1997). Determination of the fold of the core protein of hepatitis B virus by electron cryomicroscopy. *Nature,* **386**, 88–91.

Brimacombe, R. (1995). The structure of ribosomal RNA: a three-dimensional jigsaw puzzle. *Eur. J. Biochem.* **230**, 365–383.

Brünger, A. T. (1992). *X-PLOR (version 3.1): A System for X-ray Crystallography and NMR*, Yale University Press, New Haven, CT.

Cate, J. H., Gooding, A. R., Podell, E., Zhou, K., Golden, B. L., Kundrot, C. E., Cech, T. R. & Doudna, J. A. (1996). Crystal structure of a group I ribozyme domain: principles of RNA packing. *Science,* **273**, 1678–1686.

Conway, J. F., Cheng, N., Zlotnick, A., Wingfield, P. T., Stahl, S. J. & Steven, A. C. (1997). Visualization of a 4-helix bundle in the hepatitis B virus by cryo-electron microscopy. *Nature,* **386**, 91–94.

Dabrowski, M., Spahn, C. M. T. & Nierhaus, K. H. (1995). Interaction of tRNAs with the ribosome at the A and P sites. *EMBO J.* **14**, 4872–4882.

Döring, T., Mitchell, P., Osswald, M., Bochariov, D. & Brimacombe, R. (1994). The decoding region of 16 S RNA: a cross-linking study of the ribosomal A, P,

and E sites using tRNA derivatized at position 32 in the anticodon loop. *EMBO J.* **13**, 2677–2685.

Dubochet, J., Adrian, M., Chang, J. J., Homo, J. C., Lepault, J., McDonnall, A. W. & Schultz, P. (1988). Cryo-electron microscopy of vitrified specimens. *Rev. Biophys.* **21**, 129–228.

Eisenstein, M., Hardesty, B., Odom, O. W., Kudlicki, W., Kramer, G., Arad, T., Francheschi, F. & Yonath, A. (1994). Modeling and experimental study of the progression of nascent proteins in ribosomes. In *Biophysical Methods in Molecular Biology* (Pifat, G., ed.), Balaban Press.

Frank, J. (1996). *Three-dimensional Electron Microscopy of Macromolecular Assemblies*, Academic Press, San Diego, CA.

Frank, J. & Agrawal, R. K. (1998). The movement of tRNA through the ribosome. *Biophys. J.* **74**, 589–594.

Frank, J., Verschoor, A., Radermacher, M. & Wagenknecht, T. (1990). Morphologies of eubacterial and eucaryotic ribosomes as determined by three-dimensional electron microscopy. In *The Ribosome, Structure, function, Evolution* (Hill, W. E., Dahlberg, A., Garrett, R. A., Moore, P. B., Schlessinger, D. & Warner, J. R., eds), pp. 107–113, ASM Press, Washington DC.

Frank, J., Penczek, P., Grassucci, R. & Srivastava, S. (1991). Three-dimensional reconstruction of the 70 S *E. coli* ribosomes in ice: the distribution of ribosomal RNA. *J. Cell. Biol.* **115**, 597–605.

Frank, J., Verschoor, A., Li, Y., Zhu, J., Lata, R. K., Radermacher, M., Penczek, P., Grassucci, R., Agrawal, R. K. & Srivastava, S. (1995a). A model of the translational apparatus based on a three-dimensional reconstruction of the *Escherichia coli* ribosome. *Biochem. Cell Biol.* **73**, 757–765.

Frank, J., Zhu, J., Penczek, P., Li, Y., Srivastava, S., Verschoor, A., Radermacher, M., Grassucci, R., Lata, R. K. & Agrawal, R. K. (1995b). A model of protein synthesis based on cryo-electron of the *E. coli* ribosome. *Nature,* **376**, 441–444.

Green, R. & Noller, H. F. (1997). Ribosomes and translation. *Annu. Rev. Biochem.* **66**, 679–716.

Harauz, G. & van Heel, M. (1986). Exact filters for general geometry three-dimensional reconstruction. *Optik,* **73**, 146–156.

Jones, T. A., Zhou, J. Y., Cowan, S. W. & Kjeldgaard, M. (1991). Improved methods for building protein models in electron density maps and the location of errors in these models. *Acta Crystallog. sect. A,* **47**, 110–119.

Jünemann, R., Wadzack, J., Triana-Alonso, F. J., Bittner, J.-U., Caillet, J., Meinnel, T., Vanatalu, K. & Nierhaus, K. H. (1996). *In vivo* deuteration of transfer RNAs: overexpression and large-scale purification of deuterated specific tRNAs. *Nucl. Acids Res.* **24**, 907–913.

Kleywegt, G. J. & Jones, T. A. (1996). zdlMAPMAN and xdlDATAMAN: programs for reformatting, analysis and manipulation of biomacromolecular electron-density maps and reflection data sets. *Acta. Crystallog. sect. D,* **52**, 826–828.

Lata, K. R., Penczek, P. & Frank, J. (1995). Automated particle picking from electron micrographs. *Ultramicroscopy,* **58**, 381–391.

Lata, K. R., Agrawal, R. K., Penczek, P., Grassucci, R., Zhu, J. & Frank, J. (1996). Three-dimensional reconstruction of the *Escherichia coli* 30 S subunit in ice. *J. Mol. Biol.* **262**, 43–52.

Leffers, H., Kjems, J., Ostergaard, L., Larsen, N. & Garrett, R. A. (1987). Evolutionary relationships amongst archaebacteria. A comparative study of 23 S ribosomal RNAs of a sulphur-dependent extreme thermophile, an extreme halophile and a thermophilic methanogen. *J. Mol. Biol.* **195**, 43–61.

Malhotra, A. & Harvey, S. C. (1994). A quantitative model of the *E.coli* 16 S RNA in the 30 S ribosomal subunit. *J. Mol. Biol.* **240**, 308–340.

Milligan, R. A. & Unwin, P. N. T. (1986). Location of the exit channel for nascent proteins in the 80 S ribosome. *Nature,* **319**, 693–696.

Mueller, F. & Brimacombe, R. (1997). A new model for the three-dimensional folding of *Escherichia coli* 16 S ribosomal RNA. I. Fitting the RNA to a 3D electron microscopic map at 20 Å. *J. Mol. Biol.* **271**, 524–544.

Nikonov, S., Nevskaya, N., Eliseikina, I., Fomenkova, N., Nikulin, A., Ossina, N., Garber, M., Jonsson, B.-H., Briand, C., Al-Karadaghi, S., Svensson, A., Ævarsson, A. & Liljas, A. (1996). Crystal structure of the RNA binding ribosomal protein L1 from *Thermus thermophilus*. *EMBO J.* **15**, 1350–1359.

Oakes, M. I., Scheinman, A., Atha, T., Shankweiler, G. & Lake, J. A. (1990). Ribosome structure: three-dimensional locations of rRNA and proteins. In *The Ribosome, Structure, function, Evolution* (Hill, W. E., Dahlberg, A., Garrett, R. A., Moore, P. B., Schlessinger, D. & Warner, J. R., eds), pp. 180–193, ASM Press, Washington DC.

Osswald, M., Döring, T. & Brimacombe, R. (1995). The ribosomal neighbourhood of the central fold of tRNA: cross-links from position 47 to tRNA located at the A, P or E site. *Nucl. Acids Res.* **23**, 4635–4641.

Penczek, P., Grassucci, R. A. & Frank, J. (1994). The ribosome at improved resolution: new techniques for emerging and orientation refinement in 3D cryo-electron microscopy of biological particles. *Ultramicroscopy,* **53**, 251–270.

Rosen, K. V. & Zimmerman, R. A. (1997). Photoaffinity labelling of 30 S-subunit proteins S7 and S11 by 4-thiouridine-substituted $tRNA^{Phe}$ situated at the P site of *Escherichia coli* ribosomes. *RNA,* **3**, 1028–1036.

Rosen, K. V., Alexander, R. W., Wower, J. & Zimmerman, R. A. (1993). Mapping the central fold of $tRNA_2^{fMet}$ in the P site of the *Escherichia coli* ribosome. *Biochemistry,* **32**, 12802–12811.

Stark, H., Müller, F., Orlova, E. V., Schatz, M., Dube, P., Erdemir, T., Zemlin, F., Brimacombe, R. & van Heel, M. (1995). The 70 S ribosome at 23 Å resolution: fitting the ribosomal RNA. *Structure,* **3**, 815–821.

Stark, H., Orlova, E. V., Rinke-Appel, J., Jünke, N., Müller, F., Rodnina, M., Wintermeyer, W., Brimacombe, R. & van Heel, M. (1997a). Arrangement of tRNAs in pre- and posttranslational ribosomes revealed by electron cryomicroscopy. *Cell,* **88**, 19–28.

Stark, H., Rodnina, M. V., Rinke-Appel, J., Brimacombe, R., Wintermeyer, W. & van Heel, M. (1997b). Visualization of elongation factor Tu on the *Escherichia coli* ribosome. *Nature,* **389**, 403–406.

Stöffler-Meilicke, M. & Stöffler, G. (1990). Topography of the ribosomal proteins from *Escherichia coli* within the intact subunits as determined by immunoelectron microscopy and protein-protein cross-linking. In *The Ribosome, Structure, Function, Evolution* (Hill, W. E., Dahlberg, A., Garrett, R. A.,

Moore, P. B., Schlessinger, D. & Warner, J. R., eds), pp. 123–133, ASM Press, Washington, DC.
Subramanian, A. R. & Dabbs, E. R. (1980). Functional studies on ribosomes lacking protein L1 from mutant *Escherichia coli*. *Eur. J. Biochem.* **112**, 425–430.
Traut, R. R., Dey, D., Bochkariov, D. E., Oleinikov, A. V., Jokhadze, G. G., Hamman, B. & Jameson, D. (1995). Location and domain structure of *Escherichia coli* ribosomal protein L7/L12: site specific cross-linking and attachment of fluorescent probes. *Biochem. Cell Biol.* **73**, 949–958.
Verschoor, A., Warner, J. R., Srivastava, S., Grassucci, R. A. & Frank, J. (1998). Three-dimensional structure of the yeast ribosome. *Nucl. Acids Res.* **26**, 655–661.
Wadzack, J., Burkhardt, N., Jünemann, R., Diedrich, G., Nierhaus, K. H., Frank, J., Penczek, P., Meerwinck, W., Smitt, M., Willumeit, R. & Stuhrmann, H. B. (1997). Direct localization of the tRNAs within the elongating ribosome by means of neutron scattering (proton-spin contrast-variation). *J. Mol. Biol.* **266**, 343–356.
Wagenknecht, T., Grassucci, R. & Frank, J. (1988). Electron microscopy and computer image averaging of ice-embedded large ribosomal subunits from *Escherichia coli*. *J. Mol. Biol.* **199**, 137–145.
Wower, J., Sylvers, L. A., Rosen, K. V., Hixson, S. S. & Zimmermann, R. A. (1993). A model of the tRNA binding sites on the *Escherichia coli* ribosome. In *The Translational Apparatus: Structure, Function, Regulation, Evolution* (Nierhaus, K. H., Franceschi, F., Subramanian, A. P., Erdmann, V. A. & Wittmann-Liebold, B., eds), pp. 455–464, Plenum Press, New York.
Yonath, A., Leonard, K. R. & Wittmann, H. G. (1987). Tunnel in the large ribosomal subunit revealed by three-dimensional image reconstruction. *Science*, **236**, 813–815.
Zhu, J., Penczek, P. A., Schröder, R. & Frank, J. (1997). Three-dimensional reconstruction with contrast transfer function correction from energy-filtered cryoelectron micrographs: procedure and application to the 70 S *Escherichia coli* ribosome. *J. Struct. Biol.* **118**, 197–219.

Appendix: Measures of Resolution using Fourier Shell Correlation

Pawel Penczek

The resolution values given in the main paper were based on a 0.5 cutoff for the FSC curve. This value appears to be currently accepted threshold (Böttcher *et al*., 1997; Conway *et al*., 1997), although a more conservative threshold of 0.67 can be employed equally well. Sometimes the arguments for a cutoff equal to zero are put forward, supported by relatively weak statistical considerations. These arguments focus on the so called ''criterion threshold curve'' and whether it should correspond to two or rather three standard deviations (σ).

The criterion curve should be recognized as the values for a one-sided statistical test for the null hypothesis that the correlation coefficient r between two volumes calculated for a given shell in Fourier space is smaller than or equal to zero. This criterion is based on two assumptions: that the distribution of the correlation coefficient is normal (which is true for a large number of elements N considered), and that both Fourier transforms are statistically independent (which is not true, as both volumes were calculated using projections processed jointly). In this language the 2σ criterion corresponds to $\sim$0.02, and 3σ to $\sim$0.001 significance level. It is important to remember that, no matter what significance level is chosen, the correlation coefficient is tested *versus* zero value.

However, knowledge of the correlation coefficient is not very useful, one would rather like to know the signal-to-noise ratio (*SNR*) for a given frequency range. *SNR* can be approximately related to correlation coefficient, r, using a simple formula (Frank & Al-Ali, 1975):

$$SNR \cong \frac{r}{1-r} \qquad \text{(A1)}$$

Thus, $r = 1$ means infinite *SNR* or no noise in the image, while $r = 0$ means that *SNR* is zero, or that these is no signal at all. The latter does not mean that the standard deviation of the signal and that of noise are approximately of the same magnitude, as suggested by Orlova *et al*. (1997). Equation (A1) gives a choice to transfer the results of FSC into more useful *SNR* values and base the criterion on accepted *SNR* levels. It is clear that the *SNR* should be substantially higher than zero (not simply significantly higher, which for large N leads to *SNR* infinitesimally close to zero). The commonly used $SNR = 4$ threshold would result in a rather higher r threshold of 0.8, while two often-used FSC criteria of $r = 0.67$ and $r = 0.50$ correspond to $SNR = 2.0$ and $SNR = 1.0$, respectively. In each case, a one-sided statistical test for FSC being smaller or equal to the threshold chosen can be constructed. No matter what threshold is chosen (as long as it is not zero) one has to keep in mind that due to the shaky statistical basis of the estimation, the result gives us only an upper bound of the *SNR*. All we can say is that at a given resolution the *SNR* is no higher than one estimated by the FSC, but in reality it can be much lower. Thus, if one would err, it should be on a conservative side. This point is well illustrated by the resolution estimation for the high-occupancy reconstruction: using the FSC criterion with a 0.5 cutoff we estimate a resolution of 14.9 for Å, while the use of the 3σ criterion results in an estimate of 11.75 Å, close to the Nyquist frequency limit of 9.56 Å for a sampling distance of 4.78 Å.

References

Böttcher, B., Wynne, S. A. & Crowther, R. A. (1997). Determination of the fold of the core protein of hepatitis B virus by electron cryomicroscopy. *Nature*, **386**, 88–91.
Conway, J. F., Cheng, N., Zlotnick, A., Wingfield, P. T., Stahl, S. J. & Steven, A. C. (1997). Visualization of a

4-helix bundle in the hepatitis B virus capsid by cryo-electron microscopy. *Nature*, **386**, 91–94.
Frank, J. & Al-Ali, L. (1975). Signal-to-noise ratio of electron micrographs obtained by cross-correlation. *Nature*, **256**, 376–378.
Orlova, V. E., Dube, P., Harris, J. R., Beckman, E., Zemlin, F., Markl, J. & van Heel, M. (1997). Structure of keyhole limpet hemocyanin type 1 (KLH1) at 15 Å resolution by electron cryomicroscopy and angular reconstitution. *J. Mol. Biol*. **271**, 417–437.

Edited by D. Draper

(Received 19 February 1998; received in revised form 9 April 1998; accepted 10 April 1998)

Note added in proof: As this paper goes into print, we have become aware of a related article by Dube *et al*. (Dube, P., Wieske, M., Stark, H., Schatz, M., Stahl, J., Zemlin, F., Lutsch, G. & van Heel, M. (1998). *Structure*, **6**, 389–399), reporting on the structure of the 80 S rat liver ribosome. Again a tunnel is seen in the large subunit, which aligns with the *E. coli* 50 S subunit tunnel, strengthening the inference (Verschoor *et al*., 1998) that it is a universally conserved feature vitally important for ribosomal function.